AIP | Physics of Fluids

The physics of pressure variation in microchannels within corotating or static discs

Abhijit Guha and Sayantan Sengupta

Citation: Physics of Fluids **28**, 103601 (2016); doi: 10.1063/1.4963370
View online: http://dx.doi.org/10.1063/1.4963370
View Table of Contents: http://scitation.aip.org/content/aip/journal/pof2/28/10?ver=pdfcov
Published by the AIP Publishing

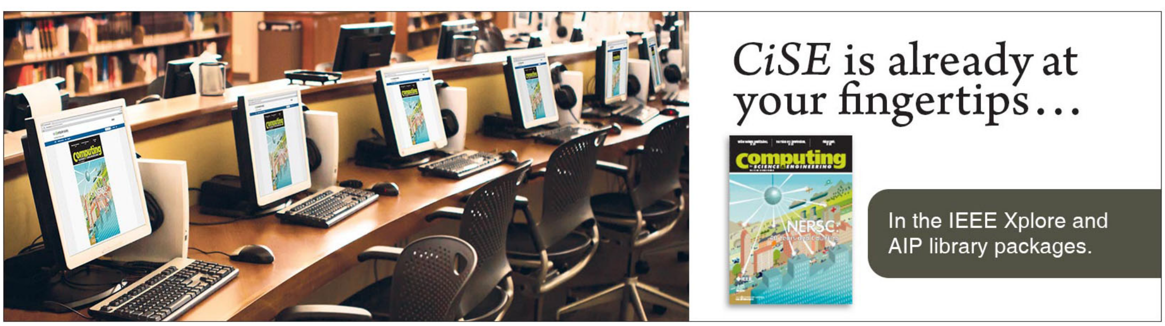

PHYSICS OF FLUIDS **28**, 103601 (2016)

The physics of pressure variation in microchannels within corotating or static discs

Abhijit Guha[a] and Sayantan Sengupta[b]
Mechanical Engineering Department, Indian Institute of Technology Kharagpur, Kharagpur 721302, India

(Received 8 April 2016; accepted 12 September 2016; published online 5 October 2016)

We formulate a comprehensive analysis for the radial pressure variation in flow through microchannels within corotating (or static) discs, which is important for its fundamental value and application potential in macrofluidic and microfluidic devices. The uniqueness and utility of the present approach emanate from our ability to describe the physics completely in terms of non-dimensional numbers and to determine quantitatively the separate roles of inertia, centrifugal force, Coriolis force, and viscous effects in the overall radial pressure difference (Δp_{io}). It is established here that the aspect ratio (ratio of inter-disc spacing and disc radius) plays only a secondary role as an independent parameter, its major role being contained within a newly identified dynamic similarity number (Ds). For radial inflow, it is shown that the magnitude of Δp_{io} decreases monotonically as the tangential speed ratio (γ) increases but exhibits a minima when Ds is varied. For radial outflow, it is shown that Δp_{io} increases monotonically as the flow coefficient (ϕ) decreases but evinces a maxima when Ds is varied. It is further shown that for the radial inflow case, the minima in the magnitude of Δp_{io} exist even when the rotational speed of the discs is reduced to zero (static discs). The demonstrated existence of these extrema (i.e., minima for radial inflow and maxima for radial outflow) creates the scope for device optimization. *Published by AIP Publishing.* [http://dx.doi.org/10.1063/1.4963370]

I. INTRODUCTION

The physics of rotating flow is a vigorously active research topic, see Refs. 1–7. All reputed monographs on rotating flow (see Refs. 8–11) devote one or more chapters on the fluid dynamics of the swirling flow adjacent to stationary or rotating discs. Many famous fluid dynamicists like von Kármán, Batchelor, Bödewadt, and Stewartson contributed to this topic yielding various perspectives. von Kármán[12] studied the flow due to a semi-infinite rotating disc, whereas Bödewadt[13] analysed the rotating flow above a static disc. While von Kármán and Bödewadt dealt with a single disc, Batchelor and Stewartson studied the flow within a rotor-stator disc cavity[14,15] formed by a stationary and a rotating disc. Many research articles are still being published on these flow configurations, e.g., Refs. 16–18 for von Kármán's flow, Refs. 19–21 for Bödewadt's flow, Refs. 22–25 for the flow within a rotor-stator disc cavity, and Refs. 26–33 for flow within corotating discs. In this paper, a new line of systematic investigation is established by exploring the important question of how pressure varies in the microchannels formed by corotating discs (or static discs), and by determining quantitatively the separate roles of various physical mechanisms, e.g., inertia, centrifugal force, Coriolis force, and viscous effects, in setting up the pressure variation. The power of similitude and dimensional analysis is combined here with the power of computational fluid dynamics (CFD) to achieve a generalized physical understanding from a large set of accurate numerical simulations. The methodology developed here may be extended to related flow configurations.

[a] Author to whom correspondence should be addressed. Electronic mail: a.guha@mech.iitkgp.ernet.in
[b] Email: sayantansengupta@iitkgp.ac.in

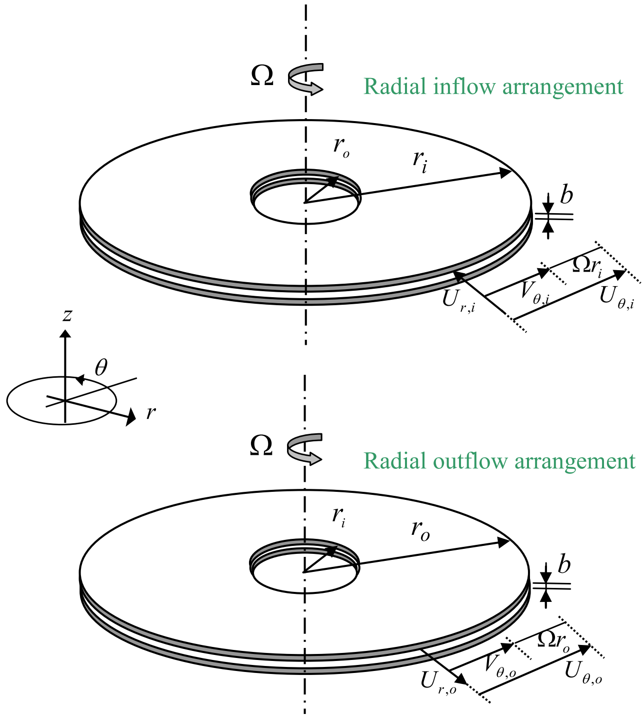

FIG. 1. Schematic diagram for the present physical configuration (the gap within the two discs, in relation to the radius, is exaggerated in the sketch for clarity) and two different flow arrangements (radial inflow and radial outflow).

Apart from its fluid dynamic significance, the present study can also be important from an engineering perspective. A few examples of disc-shaped engineering devices are Tesla disc turbine, disc pump, centrifugal microfluidic systems (e.g., lab-on-a-disc or lab-on-a-CD), micro heat sink, computer disc memory, centrifuges, gear, rotating air cleaner, and wet clutches. A thorough understanding of the fluid dynamics of pressure variation may be helpful for the design and innovative improvements in the performance of disc-based engineering devices.

Figure 1 displays the present physical configuration showing two circular discs separated axially (i.e., in the z-direction) by a distance b. Both discs are rotating about the z-axis at an angular speed Ω. For this physical configuration, two different flow arrangements, viz., radial inflow and radial outflow arrangements are widely used. For the radial inflow arrangement, the rotor inlet is situated along the periphery of the discs (i.e., at radius r_i); the rotor outlet is at the centre of the discs (at radius r_o). The working fluid is injected nearly tangentially, and the injected fluid, which passes through the inter-disc-spacing, approaches spirally towards the exhaust port located at the centre of each disc. For the radial outflow arrangement, the rotor inlet is situated at the centre of the discs (i.e., at radius r_i); the rotor outlet is along the periphery of the discs (at radius r_o). The working fluid is driven radially outward mainly because of the centrifugal force imparted on the fluid by the rotating disc-surface. The inter-disc-spacing (b) considered in the present study is of the order of 100 µm. The subtle flow physics within such micro-spacing of co-rotating discs has been established here through a comprehensive set of computational fluid dynamic (CFD) simulations, each run to a high degree of convergence (the "scaled" residual for all conserved variables is set as 10^{-10} which is much smaller than what is normally set in much of the reported CFD work). This comprehensiveness and precision have helped us to formulate a synthesis of underlying physical principles.

The present study explores the physical mechanisms of pressure variation in a microchannel within corotating discs with either radial inflow or outflow. Although a short initial attempt for understanding pressure variation in the radial inflow case was made by the authors in Figure 8 of Ref. 27, the study[27] was performed for a particular physical geometry and by varying a single, dimensional parameter (speed of rotation Ω). The present work builds upon this initial concept and systematizes and generalizes the scope and outcome of the investigation. The first generalization involves the study of the radial inflow configuration side by side with radial outflow configuration. The second generalizing aspect of the present work is that it is conducted in a fully non-dimensional framework which is versatile and flexible. Various combinations of input variables, concise representation of results, and generalized physical reflections thus become possible. The utility of the non-dimensional framework is established more fully in Section II A.

As a result of the use of the non-dimensional framework and a large number of simulations covering a wide range of the non-dimensional numbers, it has been possible to systematically examine the effect of changes in physical geometry, fluid properties, and boundary conditions on the magnitude of pressure change and on the mechanisms of pressure variation. This knowledge is new. There are other aspects in which the present paper complements and extends the work of Ref. 27. For example, the present study solves Navier-Stokes equations, and thus is able to directly assess the validity of the assumptions made in the theoretical formulation of Ref. 27 which solves a set of ordinary differential equations. Secondly, the present paper establishes how the radial variation in pressure is achieved as a balance between four components of the force, viz., centrifugal, viscous, Coriolis, and inertia. Finally, solutions are also presented here for the flow through the space between two static discs. These act as the baseline solutions which help to isolate the effects of rotation on the fluid dynamics of pressure change in the microspacing between two corotating discs.

II. MATHEMATICAL PERSPECTIVE

In this work, the subscripts i and o are used, respectively, for the inlet and outlet. As shown in Figure 1, for a given pair of discs, the positions of the inlet and outlet interchange between the radial inflow and outflow arrangements. Therefore, r_i for radial inflow and r_o for radial outflow represent the outer radius of the discs. In the flow field, a velocity vector has three components: U_r, U_θ, and U_z (i.e., absolute radial, tangential, and axial components). The symbol overbar is used to denote the depth-averaged values of the respective quantities. Thus, $\bar{U}_\theta(r) = (1/b)\int_0^b U_\theta dz$ and $\bar{U}_r(r) = (1/b)\int_0^b U_r dz$. $\bar{U}_{\theta,i}$ is the value of $\bar{U}_\theta(r)$ at the inlet, i.e., at $r = r_i$. Similarly, $\bar{U}_{r,i}$ is the value of $\bar{U}_r(r)$ at the inlet. The depth-averaging may also be performed on the pressure such that $\bar{p}(r) = (1/b)\int_0^b p dz$.

In the present study, two quantities are used to denote pressure difference, viz., Δp_{io} and $\Delta p_{net}(r)$. Δp_{io} is called the overall radial pressure difference and is the difference between the depth-averaged pressure at outlet and that at inlet. A positive value of Δp_{io} signifies that pressure increases from the inlet to the outlet. $\Delta p_{net}(r)$ is termed the local net pressure difference and is the difference between the depth-averaged local pressure at a given radial location and that at inlet.

The present study is conducted for steady, laminar, axisymmetric, incompressible flow of a Newtonian fluid with constant density and viscosity. The results are expressed in a relative frame of reference in which the observer is rotating at the same angular velocity as that of the disc (Ω). The relations between the components of velocity in absolute frame (U_r, U_z, and U_θ) and those in the relative frame (V_r, V_z, and V_θ) are as follows: $U_r = V_r; U_z = V_z; U_\theta = (V_\theta + \Omega r)$. In this relative frame of reference, the (dimensional form of) r-momentum equation[10] is as follows:

$$\frac{\partial p}{\partial r} = \left(\frac{\rho V_\theta^2}{r} - \rho V_r\frac{\partial V_r}{\partial r} - \rho V_z\frac{\partial V_r}{\partial z}\right) + 2\rho\Omega V_\theta + \rho\Omega^2 r + \mu\left[\frac{1}{r}\frac{\partial}{\partial r}(r\frac{\partial V_r}{\partial r}) - \frac{V_r}{r^2} + \frac{\partial^2 V_r}{\partial z^2}\right]. \quad (1)$$

Equation (1) can easily be interpreted as a relation between the radial pressure gradient ($\frac{\partial p}{\partial r}$) and the terms obtained from various forces. The overall radial pressure difference Δp_{io} is obtained by integrating Equation (1). The integral form of Equation (1) is as follows:

$$\begin{aligned}\frac{1}{b}\int_{r_i}^{r_o}\int_0^b \frac{\partial p}{\partial r}dzdr &= \int_{r_i}^{r_o}\left(\frac{1}{b}\int_0^b\left(\frac{\rho V_\theta^2}{r} - \rho V_r\frac{\partial V_r}{\partial r} - \rho V_z\frac{\partial V_r}{\partial z}\right)dz\right)dr \\ &+ \int_{r_i}^{r_o}\left(\frac{1}{b}\int_0^b(2\rho\Omega V_\theta)dz\right)dr + \int_{r_i}^{r_o}\left(\frac{1}{b}\int_0^b(\rho\Omega^2 r)dz\right)dr \\ &+ \int_{r_i}^{r_o}\left(\frac{1}{b}\int_0^b\left(\mu\left[\frac{1}{r}\frac{\partial}{\partial r}(r\frac{\partial V_r}{\partial r}) - \frac{V_r}{r^2} + \frac{\partial^2 V_r}{\partial z^2}\right]\right)dz\right)dr.\end{aligned} \quad (2)$$

The physical interpretations of various terms in Equation (2) are provided below. In the left hand side of Equation (2), the term $\frac{1}{b}\int_{r_i}^{r_o}\int_0^b \frac{\partial p}{\partial r}\delta z\delta r$ signifies the (depth-averaged) overall radial pressure difference, i.e., Δp_{io}. In the right hand side of Equation (2), the first term indicates the contribution of inertia force, $\Delta p_{io,inertia}$; the second term displays the contribution of Coriolis force, $\Delta p_{io,Coriolis}$; the third term indicates the contribution of centrifugal force, $\Delta p_{io,centrifugal}$; and the fourth term gives the contribution of viscous effect, $\Delta p_{io,viscous}$.

A study of Equation (2) sheds light on the nature of variation of the four components of Δp_{io} with various flow and geometric parameters. A few observations are listed below. (i) Out of the four components, only $\Delta p_{io,viscous}$ depends directly on the fluid viscosity μ, and $\Delta p_{io,centrifugal}$ does not depend at all on μ. The two other components are affected indirectly by the magnitude of μ through the effects of viscosity on the velocity field, viz., the spatial distributions of V_θ and V_r. A reduction in μ (i.e., an increase in the non-dimensional number Ds introduced in Sec. II A) increases $\Delta p_{io,inertia}$. (ii) $\Delta p_{io,viscous}$ depends only on the radial velocity V_r and not on the relative tangential velocity V_θ, the exactly opposite dependence being true for $\Delta p_{io,Coriolis}$. $\Delta p_{io,centrifugal}$ does not depend either on V_θ or V_r, while $\Delta p_{io,inertia}$ depends on both. (iii) The speed of rotation Ω appears directly in the centrifugal and Coriolis components (the effect on the centrifugal component being the strongest because it appears as Ω^2). Ω only indirectly affects the viscous and inertia components through its effect on the velocity field (V_θ is more affected than V_r, and hence, the effect of Ω is relatively greater on inertia than the viscous component). (iv) The inter-disc spacing b most strongly affects the viscous component $\Delta p_{io,viscous}$; its effects on the other three components are mainly through the velocity field (although the inertia component $\Delta p_{io,inertia}$ contains the velocity gradient $\partial V_r/\partial z$, the gradient is multiplied by a small quantity V_z). (v) The radial variation in V_θ can be complex,[27,30] and consequently there can be subtle variation in the magnitude and sign of the Coriolis component $\Delta p_{io,Coriolis}$, which depends on the cross-product of the relative tangential velocity V_θ and angular velocity of the discs. The sign of V_θ does not bring similar complexity in the variation of $\Delta p_{io,inertia}$, since it appears as a squared quantity (i.e., as V_θ^2). The qualitative features described in this paragraph will be useful later for interpreting the computed results.

A. Similitude and non-dimensionalization

The flow solutions are obtained in this work by the application of a computational fluid dynamics (CFD) software which is described in Section III. Here, we give a brief account of a mathematical formulation that serves two principal purposes. First of all, with the help of this non-dimensional mathematical formulation, the CFD results can be post-processed and recast in terms of appropriate non-dimensional numbers. This allows generalization of the underlying scientific principles and significant conciseness in the presentation of the output results. Secondly, the non-dimensional mathematical formulation allows one to undertake a scale analysis which enhances physical understanding and reveals the relative importance of the various terms in an equation. With this, it becomes easier to comprehend the large amount of data generated through CFD and to make appropriate physical reflections on the computed results.

In one of our previous publications,[26] we have formulated a systematic dimensional analysis and appropriate scaling laws for the radial inflow arrangement (Figure 1). Based on this, five input non-dimensional numbers are used for the radial inflow arrangement. These are radius ratio $\hat{r}_o$ ($\hat{r}_o \equiv r_o/r_i$), aspect ratio $\hat{b}$ ($\hat{b} \equiv b/r_i$), tangential speed ratio at inlet γ ($\gamma \equiv \bar{U}_{\theta,i}/\Omega r_i$), flow angle at inlet α ($\alpha \equiv \tan^{-1}(\left|\bar{U}_{r,i}\right|/\bar{U}_{\theta,i})$), and dynamic similarity number Ds ($Ds \equiv \left|\bar{U}_{r,i}\right| b^2/(\nu\ r_i)$). The symbol ν denotes the kinematic viscosity of the fluid which is the ratio of dynamic viscosity μ and density ρ. For the usual radial inflow configuration, the fluid enters nearly tangentially, i.e., the value of the flow angle at inlet α would be small. In addition to the above non-dimensional numbers, the relevant non-dimensional variables required for the present analysis are given in Table I.

For the radial outflow arrangement (Figure 1), the four relevant input non-dimensional numbers are radius ratio $\hat{r}_i$ ($\hat{r}_i \equiv r_i/r_o$), aspect ratio $\hat{b}$ ($\hat{b} \equiv b/r_o$), flow coefficient at inlet ϕ ($\phi \equiv \bar{U}_{r,i}/(\Omega r_i)$), and dynamic similarity number Ds ($Ds \equiv \bar{U}_{r,i}\ b^2/(\nu\ r_i)$). For the case of radial outflow, the flow angle at inlet α is not treated as a variable since, from practical considerations, its usual value would

TABLE I. Non-dimensionalisation schemes for radial inflow and outflow arrangements.

Dimensional variable	Symbol for the corresponding non-dimensional variable	Expression of the non-dimensional variable for radial inflow arrangement	Expression of the non-dimensional variable for radial outflow arrangement
r	$\hat{r}$	r/r_i	r/r_o
z	$\hat{z}$	z/b	z/b
U_r	$\hat{U}_r$	$U_r/\lvert\bar{U}_{r,i}\rvert$	$U_r/\bar{U}_{r,i}$
U_θ	$\hat{U}_\theta$	$U_\theta/(\Omega r_i)$	$U_\theta/(\Omega r_o)$
U_z	$\hat{U}_z$	$(U_z r_i)/(\lvert\bar{U}_{r,i}\rvert b)$	$(U_z r_o)/(\bar{U}_{r,i} b)$
p	$\hat{p}$	$p/(\rho\bar{U}^2_{\theta,i})$	$p/(\rho\Omega^2 r_o^2)$
Δp_{io}	$\Delta\hat{p}_{io}$	$\Delta p_{io}/(\rho\bar{U}^2_{\theta,i})$	$\Delta p_{io}/(\rho\Omega^2 r_o^2)$
$\Delta p_{net}(r)$	$\Delta\hat{p}_{net}(r)$	$\Delta p_{net}(r)/(\rho\bar{U}^2_{\theta,i})$	$\Delta p_{net}(r)/(\rho\Omega^2 r_o^2)$
$\Delta p_{io,inertia}$	$\Delta\hat{p}_{io,inertia}$	$\Delta p_{io,inertia}/(\rho\bar{U}^2_{\theta,i})$	$\Delta p_{io,inertia}/(\rho\Omega^2 r_o^2)$
$\Delta p_{io,Coriolis}$	$\Delta\hat{p}_{io,Coriolis}$	$\Delta p_{io,Coriolis}/(\rho\bar{U}^2_{\theta,i})$	$\Delta p_{io,Coriolis}/(\rho\Omega^2 r_o^2)$
$\Delta p_{io,centrifugal}$	$\Delta\hat{p}_{io,centrifugal}$	$\Delta p_{io,centrifugal}/(\rho\bar{U}^2_{\theta,i})$	$\Delta p_{io,centrifugal}/(\rho\Omega^2 r_o^2)$
$\Delta p_{io,viscous}$	$\Delta\hat{p}_{io,viscous}$	$\Delta p_{io,viscous}/(\rho\bar{U}^2_{\theta,i})$	$\Delta p_{io,viscous}/(\rho\Omega^2 r_o^2)$

be 90° (i.e., the inlet velocity is in the radial direction). The non-dimensional variables required for analysing the fluid dynamics of radial outflow are also given in Table I.

We have already mentioned that the non-dimensional mathematical formulation allows one to undertake a scale analysis which enhances physical understanding and reveals the relative importance of the various terms in an equation. In this spirit, two sets of non-dimensional governing equations are given below, one for the radial inflow arrangement and the second for the radial outflow arrangement.

The non-dimensional governing equations for the radial inflow arrangement are as follows:

$$\frac{1}{\hat{r}}\frac{\partial(\hat{r}\hat{U}_r)}{\partial\hat{r}} + \frac{\partial\hat{U}_z}{\partial\hat{z}} = 0, \tag{3}$$

$$\hat{U}_r\frac{\partial\hat{U}_r}{\partial\hat{r}} + \hat{U}_z\frac{\partial\hat{U}_r}{\partial\hat{z}} - \frac{\hat{U}_\theta^2}{\hat{r}(\gamma\tan\alpha)^2} = -\frac{1}{(\tan\alpha)^2}\frac{\partial\hat{p}}{\partial\hat{r}} + \frac{1}{Ds}\left[\frac{\partial^2\hat{U}_r}{\partial\hat{z}^2} + \hat{b}^2\left(\frac{1}{\hat{r}}\frac{\partial}{\partial\hat{r}}(\hat{r}\frac{\partial\hat{U}_r}{\partial\hat{r}}) - \frac{\hat{U}_r}{\hat{r}^2}\right)\right], \tag{4}$$

$$\hat{U}_r\frac{\partial\hat{U}_\theta}{\partial\hat{r}} + \hat{U}_z\frac{\partial\hat{U}_\theta}{\partial\hat{z}} + \frac{\hat{U}_r\hat{U}_\theta}{\hat{r}} = \frac{1}{Ds}\left[\frac{\partial^2\hat{U}_\theta}{\partial\hat{z}^2} + \hat{b}^2\left(\frac{1}{\hat{r}}\frac{\partial}{\partial\hat{r}}(\hat{r}\frac{\partial\hat{U}_\theta}{\partial\hat{r}}) - \frac{\hat{U}_\theta}{\hat{r}^2}\right)\right], \tag{5}$$

$$\hat{U}_r\frac{\partial\hat{U}_z}{\partial\hat{r}} + \hat{U}_z\frac{\partial\hat{U}_z}{\partial\hat{z}} = -\frac{1}{\hat{b}^2(\tan\alpha)^2}\left(\frac{\partial\hat{p}'}{\partial\hat{z}}\right) + \frac{1}{Ds}\left[\hat{b}^2\left(\frac{1}{\hat{r}}\frac{\partial}{\partial\hat{r}}(\hat{r}\frac{\partial\hat{U}_z}{\partial\hat{r}})\right) + \frac{\partial^2\hat{U}_z}{\partial\hat{z}^2}\right]. \tag{6}$$

The non-dimensional governing equations for the radial outflow arrangement are as follows:

$$\frac{1}{\hat{r}}\frac{\partial(\hat{r}\hat{U}_r)}{\partial\hat{r}} + \frac{\partial\hat{U}_z}{\partial\hat{z}} = 0, \tag{7}$$

$$\hat{U}_r\frac{\partial\hat{U}_r}{\partial\hat{r}} + \hat{U}_z\frac{\partial\hat{U}_r}{\partial\hat{z}} - \frac{1}{\psi^2}\frac{\hat{U}_\theta^2}{\hat{r}} = -\frac{1}{\psi^2}\frac{\partial\hat{p}}{\partial\hat{r}} + \frac{1}{Ds^*}\left[\frac{\partial^2\hat{U}_r}{\partial\hat{z}^2} + \hat{b}^2\left(\frac{1}{\hat{r}}\frac{\partial}{\partial\hat{r}}(\hat{r}\frac{\partial\hat{U}_r}{\partial\hat{r}}) - \frac{\hat{U}_r}{\hat{r}^2}\right)\right], \tag{8}$$

$$\hat{U}_r\frac{\partial\hat{U}_\theta}{\partial\hat{r}} + \hat{U}_z\frac{\partial\hat{U}_\theta}{\partial\hat{z}} + \frac{\hat{U}_r\hat{U}_\theta}{\hat{r}} = \frac{1}{Ds^*}\left[\frac{\partial^2\hat{U}_\theta}{\partial\hat{z}^2} + \hat{b}^2\left(\frac{1}{\hat{r}}\frac{\partial}{\partial\hat{r}}(\hat{r}\frac{\partial\hat{U}_\theta}{\partial\hat{r}}) - \frac{\hat{U}_\theta}{\hat{r}^2}\right)\right], \tag{9}$$

$$\hat{U}_r\frac{\partial\hat{U}_z}{\partial\hat{r}} + \hat{U}_z\frac{\partial\hat{U}_z}{\partial\hat{z}} = -\frac{1}{\hat{b}^2\psi^2}\left(\frac{\partial\hat{p}'}{\partial\hat{z}}\right) + \frac{1}{Ds^*}\left[\hat{b}^2\left(\frac{1}{\hat{r}}\frac{\partial}{\partial\hat{r}}(\hat{r}\frac{\partial\hat{U}_z}{\partial\hat{r}})\right) + \frac{\partial^2\hat{U}_z}{\partial\hat{z}^2}\right]. \tag{10}$$

Equations (3)-(6) and (7)-(10) are obtained from Navier-Stokes equations in cylindrical coordinate, invoking the assumptions mentioned above. Present study considers laminar flow (for which $Ds < 10$, see Ref. 27). g_θ and g_r are zero for the assumed orientation of the discs. In Equations (6) and (10), p' is the modified pressure, i.e., $(p - \rho g_z z)$. In Equations (8)-(10), two additional non-dimensional parameters, ψ and Ds^*, are used. The expressions of ψ and Ds^* are as follows:

$$\begin{aligned} \psi &= \phi\, \hat{r}_i \\ Ds^* &= Ds\, \hat{r}_i. \end{aligned} \tag{11}$$

The boundary conditions for the radial inflow arrangement are given below

$$\text{at } \hat{z} = 0 \text{ and } 1, \qquad \hat{U}_r = 0,\ \hat{U}_\theta = \hat{r},\ \hat{U}_z = 0, \tag{12}$$

$$\text{at } \hat{r} = 1, \qquad \hat{U}_r = \hat{U}_{r,i},\ \hat{U}_\theta = \hat{U}_{\theta,i},\ \hat{U}_z = 0, \tag{13}$$

$$\text{at } \hat{r} = {}^{r_o}/_{r_i}, \qquad \hat{p} = 0. \tag{14}$$

The surfaces of the two discs are located at $\hat{z} = 0$ and $\hat{z} = 1$; Equation (12) refers to the no slip boundary condition. At inlet, both radial and tangential components of velocity are specified. (Both $\hat{U}_{r,i}$ and $\hat{U}_{\theta,i}$ are independent of θ.) At outlet, a zero gauge pressure is specified.

The boundary conditions for the radial outflow arrangement are given below

$$\text{at } \hat{z} = 0 \text{ and } 1, \qquad \hat{U}_r = 0,\ \hat{U}_\theta = \hat{r},\ \hat{U}_z = 0, \tag{15}$$

$$\text{at } \hat{r} = {}^{r_i}/_{r_o}, \qquad \hat{U}_r = \hat{U}_{r,i},\ \hat{U}_\theta = 0,\ \hat{U}_z = 0, \tag{16}$$

$$\text{at } \hat{r} = 1, \qquad \hat{p} = 0. \tag{17}$$

A study of Equations (4)-(6) and (8)-(10) shows that wherever the aspect ratio ($\hat{b}$) appears as a separate non-dimensional number, independent of the dynamic similarity number Ds or Ds^*, it appears as a squared quantity. Its physical significance will be revealed later in Section IV A 1.

III. COMPUTATIONAL FRAMEWORK

Dimensional Navier-Stokes equations are solved by applying the Fluent software which employs the finite-volume discretization method.[34] The integral form of Navier-Stokes equations is considered at each mapped, quadrilateral cell of the numerical grid to obtain a set of coupled nonlinear algebraic equations that are pseudolinearized and solved.[35] Axi-symmetric swirl model[34] is implemented in a two-dimensional interface, and double precision arithmetic is adopted for all numerical calculations given in this paper. Second order upwind scheme for discretizing the advection terms and the "Standard" scheme[34] for interpolating pressure are utilized. An implicit[36] time-marching method is used. Under-relaxation factors for momentum (radial and axial components), swirl (tangential component), pressure, density, and body force are chosen as 0.7, 0.9, 0.3, 1, and 1, respectively. The convergence criterion for the maximum "scaled" residual[34] for all conserved variables is set as 10^{-10}.

A grid independence test has been carried out (Table II showing a few pertinent details for uniform velocity distribution at inlet), and based on this study, a total 12 500 (125 × 100) mapped, quadrilateral computational cells are used for the results presented in this paper. The grids are constructed carefully as per Ref. 30. The grids are distributed in r and z directions in accordance with the difference in the flow physics in the two directions. The grid distribution in the z-direction is non-uniform with very small grid size close to the surfaces of the two discs (to capture the velocity gradient on the surface accurately) and with progressively larger grid size as one moves away from

TABLE II. Grid independence test.

Grid distribution	Number of grids in the r and z directions	Total number of grids	$\Delta\hat{p}_{io}$ [$\equiv \Delta p_{io}/(\rho \bar{U}_{\theta,i}^2)$] for radial inflow arrangement ($\hat{b} = 0.008, \hat{r}_o = 0.528, \alpha = 6.2°, \gamma = 1.25, Ds = 1.26$)	$\Delta\hat{p}_{io}$ [$\equiv \Delta p_{io}/(\rho \Omega^2 r_o^2)$] for radial outflow arrangement ($\hat{b} = 0.008, \hat{r}_i = 0.528, \alpha = 90°, Ds = 2.39, \phi = 0.26$)
Coarse	(75 × 50)	3 750	−0.615	0.121
Standard	(125 × 100)	12 500	−0.616	0.120
Fine	(200 × 150)	30 000	−0.616	0.120

the surfaces to the middle of the inter-disc gap (with a successive ratio of 1.05). Guha and Sengupta[30] have shown that when there is no z-dependence in the applied boundary conditions at inlet for the radial and tangential velocities, both velocities change very rapidly within a very short radial distance from the inlet, within which the z-profiles of both velocities are created from their uniform values at inlet. In order to capture this effect properly, the grids in the radial direction are divided into two zones—non-uniform and uniform. Near the inlet, non-uniform boundary-layer-type grids with 25 rows in the radial direction are used. The size of the first grid is 0.001 mm and the successive ratio of the geometric progression series is 1.2. The rest of the radial extent up to the outlet is meshed uniformly with 100 grid points. The non-dimensional input parameters, used in the representative computations for radial inflow and outflow arrangements, are provided in Table II. Table II shows the computed values of $\Delta\hat{p}_{io}$ for three different grid distributions (coarse, standard, and fine). For both flow arrangements, a marginal change of $\Delta\hat{p}_{io}$ is observed after attaining a grid distribution of 125×100 (the distribution is referred as standard in Table II). All results given in this paper are obtained by using the grid distribution of 125×100.

IV. RESULTS AND DISCUSSION

For radial inflow, $\Delta\hat{p}_{io}$ depends on the five non-dimensional numbers: $\hat{r}_o, \hat{b}, \gamma, Ds$, and α [see Equations (3)-(6)]. For radial outflow, $\Delta\hat{p}_{io}$ depends on the four non-dimensional numbers: $\hat{r}_i, \hat{b}, \phi$, and Ds [see Equations (7)-(10)]. It is to be recognized that the same dimensional quantity may be involved in more than one non-dimensional numbers. As an example, b, the gap between two consecutive discs, appears both in aspect ratio, $\hat{b}$, and dynamic similarity number, Ds. Therefore, a non-dimensional study, in which the effect of varying a non-dimensional number is to be found while keeping other non-dimensional numbers fixed, can be performed in a number of ways. Suppose we want to study the effect of dynamic similarity number. In a computational study, this can be achieved simply by altering the fluid viscosity μ, since μ appears only in the definition of Ds. Therefore, Ds can be varied very simply by this method while keeping all other non-dimensional numbers fixed. This is the method adopted in the present study. On the other hand, if one is to embark upon an experimental study, this method alone may not be sufficient or appropriate as the available values of μ will be restricted by the values of a real property of suitable fluids. Hence, a number of (raw) dimensional quantities may need to be simultaneously adjusted to vary Ds continuously while keeping other non-dimensional numbers fixed.

A. Radial inflow arrangement

Figure 1 shows the physical configuration, and Figures 2-5 and Table III show representative results for the radial inflow case. Quantities like pressure and pressure difference are non-dimensionalized by $\rho\bar{U}_{\theta,i}^2$. Since $\rho\bar{U}_{\theta,i}^2$ is constant for all simulations shown in Figures 2-5, non-dimensional pressure differences shown in the figures are directly proportional to their dimensional counterparts. Out of the four components of pressure difference, only the non-dimensional centrifugal component can be expressed by an explicit algebraic relation: $\Delta\hat{p}_{io,centrifugal} = (\hat{r}_o^2 - 1)/(2\gamma^2)$.

In the present study, we focus our attention to the two most important non-dimensional numbers, viz., Ds and γ. The secondary role of aspect ratio $\hat{b}$, as an additional non-dimensional number outside Ds, is also revealed here. Ds and γ are important non-dimensional numbers; they contain physical variables such as fluid viscosity, inter-disc spacing, and the rotational speed which, one can anticipate, will have important effect on the fluid dynamics. For all the results presented here, fixed values of radius ratio of the rotor ($\hat{r}_o$) and the flow angle at inlet to the rotor (α) are used. We have assumed $\hat{r}_o = 0.528$ and $\alpha = 6.2°$ (i.e., 0.11 radian), the values adopted in the experimental study of Ref. 32. Sample computations were also repeated at other values of $\hat{r}_o$ and α, but it was found that they do not reveal any new physics; hence, they are not reported here.

The present section is divided into three subsections for streamlining the physical understanding. Section IV A 1, with Figures 2 and 3 and Table III, presents the variation in the overall radial pressure difference (Δp_{io}), Section IV A 2, with Figure 4, gives the variation in local net pressure difference

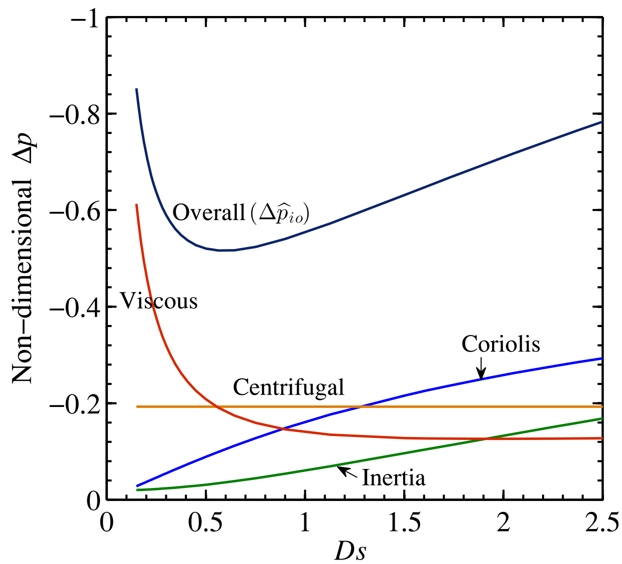

FIG. 2. Contribution of various forces to produce the overall radial pressure difference $\Delta\hat{p}_{io}$ over a range of dynamic similarity number Ds: prediction of the present CFD simulations for radial inflow. ($\hat{r}_o = 0.528, \hat{b} = 0.008, \gamma = 1.37, \alpha = 6.2°$, and parabolic velocity distribution at inlet: $U_{\theta,i} = \bar{V}_{\theta,i}[6(z/b)(1-z/b)] + \Omega r_i, U_{r,i} = \bar{U}_{r,i}[6(z/b)(1-z/b)]$. Pressure differences are non-dimensionalized by $\rho\bar{U}^2_{\theta,i}$. Each curve contains data from 50 separate CFD simulations, with appropriate higher resolution close to the minima.)

$\Delta p_{net}(r)$, and Section IV A 3, with Figure 5, discusses the baseline solutions when the discs are static. The role of the four components of force is explained in all three subsections.

1. Physical mechanisms for the overall pressure difference, $\Delta\hat{p}_{io}$

First of all, we investigate the role of Ds while keeping all other non-dimensional numbers fixed. In order to generate a high-definition set of comprehensive results, full CFD simulations are

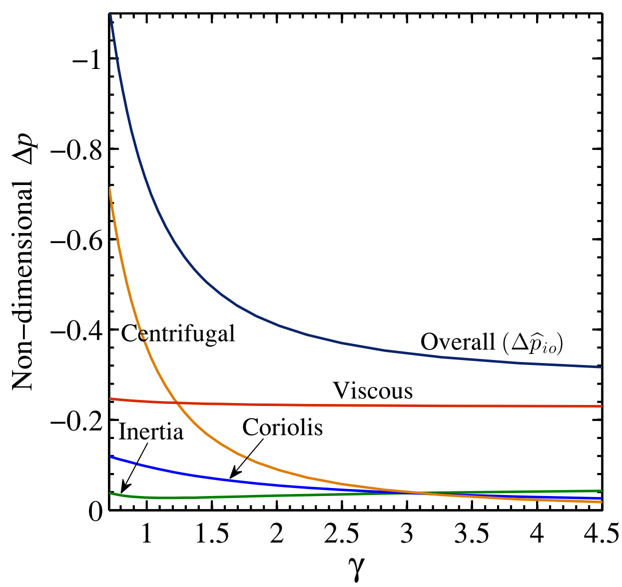

FIG. 3. Contribution of various forces to produce the overall radial pressure difference $\Delta\hat{p}_{io}$ over a range of tangential speed ratio at inlet γ: prediction of the present CFD simulations for radial inflow. ($\hat{r}_o = 0.528, \hat{b} = 0.008, Ds = 0.43, \alpha = 6.2°$, and parabolic velocity distribution at inlet: $U_{\theta,i} = \bar{V}_{\theta,i}[6(z/b)(1-z/b)] + \Omega r_i, U_{r,i} = \bar{U}_{r,i}[6(z/b)(1-z/b)]$. Pressure differences are non-dimensionalized by $\rho\bar{U}^2_{\theta,i}$. Each curve contains data from 50 separate CFD simulations.)

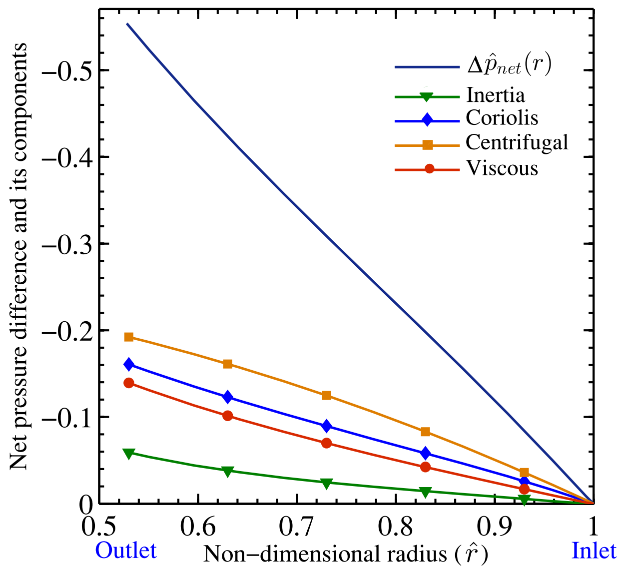

FIG. 4. Radial variation of local net pressure difference $\Delta\hat{p}_{net}(r)$ and its components: prediction of the present CFD simulations for radial inflow. ($\hat{r}_o = 0.528, \hat{b} = 0.008, Ds = 1, \gamma = 1.37, \alpha = 6.2°$, and parabolic velocity distribution at inlet: $U_{\theta,i} = \bar{V}_{\theta,i}[6(z/b)(1-z/b)] + \Omega r_i, U_{r,i} = \bar{U}_{r,i}[6(z/b)(1-z/b)]$. Pressure differences are non-dimensionalized by $\rho\bar{U}^2_{\theta,i}$. There are 125 grid points between the inlet and the outlet.)

run at each of 50 different values of Ds, with appropriate local clustering of data points for higher quantitative resolution in the region of greater qualitative significance. Figure 2 represents the final outcome of this labour-intensive computation.

Figure 2 shows the variation of $\Delta\hat{p}_{io}$ and its four components $\Delta\hat{p}_{io,inertia}$, $\Delta\hat{p}_{io,Coriolis}$, $\Delta\hat{p}_{io,centrifugal}$, and $\Delta\hat{p}_{io,viscous}$ with Ds. The negative values of $\Delta\hat{p}_{io}$ signify that pressure decreases from the inlet to the outlet. It can be seen that the curve corresponding to the variation of $\Delta\hat{p}_{io}$ is bucket-shaped, and

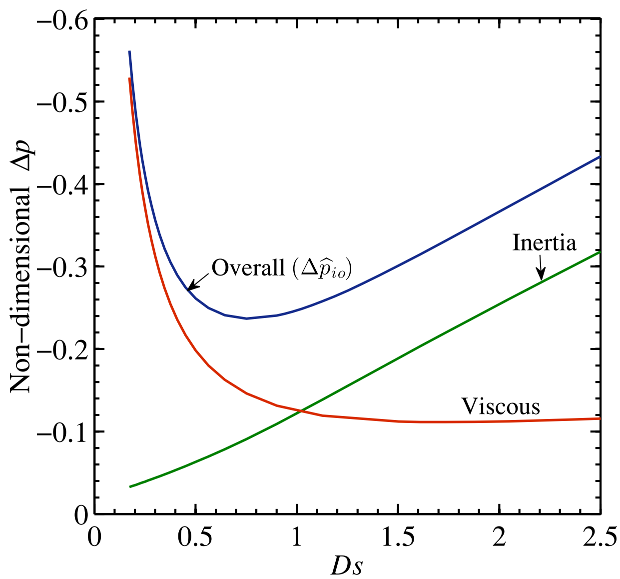

FIG. 5. Contribution of various forces within two static discs to produce the overall radial pressure difference $\Delta\hat{p}_{io}$ over a range of dynamic similarity number Ds: prediction of the present CFD simulations for radial inflow. ($\hat{r}_o = 0.528, \hat{b} = 0.008, \alpha = 6.2°$, and parabolic velocity distribution at inlet: $U_{\theta,i} = \bar{V}_{\theta,i}[6(z/b)(1-z/b)] + \Omega r_i, U_{r,i} = \bar{U}_{r,i}[6(z/b)(1-z/b)]$. Pressure differences are non-dimensionalized by $\rho\bar{U}^2_{\theta,i}$. Each curve contains data from 50 separate CFD simulations, with appropriate higher resolution close to the minima.)

TABLE III. The role of aspect ratio ($\hat{b}$) as a separate dimensionless number, independent of dynamic similarity number (Ds), in determining three representative output parameters (CFD simulations are performed for $\hat{r}_o = 0.528, \gamma = 1.37, \alpha = 6.2°$, and parabolic velocity distribution at inlet).

Ds	$\hat{b}$	$\Delta\hat{p}_{io}\,[\equiv \Delta p_{io}/(\rho \overline{U}_{\theta,i}^2)]$	$\overline{U}_{\theta,o}$	$\overline{U}_{r,o}$
	0.004	0.533	0.689	−1.893
0.43	0.008	0.533	0.689	−1.893
	0.016	0.533	0.689	−1.893
	0.004	0.783	1.345	−1.895
2.5	0.008	0.783	1.345	−1.895
	0.016	0.783	1.345	−1.895

the magnitude of $\Delta\hat{p}_{io}$ is minimum at a certain Ds (around 0.56 for the present case). For both small and large values of Ds, the magnitude of $\Delta\hat{p}_{io}$ is large. The physical reason behind the bucket-shape of $\Delta\hat{p}_{io}$ versus Ds curve can be understood in terms of the quantitative variation of the four components of $\Delta\hat{p}_{io}$. $\Delta\hat{p}_{io,centrifugal}$ does not vary with a change in Ds. ($\Delta\hat{p}_{io,centrifugal}$ depends on $\hat{r}_o$ and γ. Both $\hat{r}_o$ and γ are fixed in this case.) Secondly, with an increase in Ds, the magnitudes of both $\Delta\hat{p}_{io,inertia}$ and $\Delta\hat{p}_{io,Coriolis}$ increase; whereas, the magnitude of $\Delta\hat{p}_{io,viscous}$ decreases. Thirdly, at a small value of Ds, the magnitudes of both $\Delta\hat{p}_{io,inertia}$ and $\Delta\hat{p}_{io,Coriolis}$ are small, whereas, the magnitude of $\Delta\hat{p}_{io,viscous}$ is large. Finally, at a large Ds, the magnitudes of both $\Delta\hat{p}_{io,inertia}$ and $\Delta\hat{p}_{io,Coriolis}$ overtake the magnitude of $\Delta\hat{p}_{io,viscous}$.

It can be summarised that at a small value of Ds, a large $\Delta\hat{p}_{io}$ occurs because of the large $\Delta\hat{p}_{io,viscous}$. On the other hand, at a comparatively greater Ds, a large $\Delta\hat{p}_{io}$ occurs from a combined effect of $\Delta\hat{p}_{io,inertia}, \Delta\hat{p}_{io,Coriolis}$, and $\Delta\hat{p}_{io,centrifugal}$. This subtle fluid dynamics is responsible for the bucket-shaped $\Delta\hat{p}_{io}$ versus Ds curve. It is to be noted that Ds is a product of aspect ratio and the term $|\bar{U}_{r,i}|\, b/\nu$. The term $|\bar{U}_{r,i}|\, b/\nu$ can be interpreted as a Reynolds number based on the average radial velocity at inlet and inter-disc-spacing. Keeping the aspect ratio fixed, an increase in Ds, therefore, should lead to an increase in the ratio of inertial and viscous contributions. In fact, Figure 2 shows that an increase in Ds leads to an increase in $\Delta\hat{p}_{io,inertia}$ and a simultaneous decrease in $\Delta\hat{p}_{io,viscous}$.

We now investigate the role of γ while keeping all other non-dimensional numbers fixed. γ is defined as: $\gamma = \bar{U}_{\theta,i}/(\Omega r_i)$. The absolute tangential velocity at the inlet of the rotor, $\bar{U}_{\theta,i}$, is fixed by the design of the inlet nozzle, and r_i is fixed for a particular rotor. Therefore, in order to understand the fluid dynamics of the rotational flow, γ in this study is varied by altering the rotational speed Ω. In order to generate a high-definition set of comprehensive results, full CFD simulations are run at each of 50 different values of γ. Figure 3 represents the final outcome of this labour-intensive computation.

Figure 3 shows the variation of $\Delta\hat{p}_{io}$ and its four components $\Delta\hat{p}_{io,inertia}$, $\Delta\hat{p}_{io,Coriolis}$, $\Delta\hat{p}_{io,centrifugal}$, and $\Delta\hat{p}_{io,viscous}$ with γ. It can be seen that the magnitude of $\Delta\hat{p}_{io}$ increases with a decrease in γ and the rate of the increase is greater at comparatively smaller values of γ. Since $\Delta\hat{p}_{io,centrifugal}$ is inversely proportional to the square of γ, the value of $\Delta\hat{p}_{io,centrifugal}$ increases rapidly with a decrease in γ and at small $\gamma, \Delta\hat{p}_{io,centrifugal}$ becomes the major contributor to overall $\Delta\hat{p}_{io}$.

Figure 3 shows that at the selected value of Ds, the magnitude of $\Delta\hat{p}_{io,viscous}$ is significant at all values of γ. Equation (4) shows that γ is not present in the viscous term; this is reflected in Figure 3. Moreover, it is found in the CFD simulations that the radial velocity field within the inter-disc-spacing of the present physical configuration is weakly dependent on γ.

For the selected Ds of Figure 3, both $\Delta\hat{p}_{io,Coriolis}$ and $\Delta\hat{p}_{io,inertia}$ are small, which is consistent with the message contained in Figure 2. Figure 2 also suggests that if the curves in Figure 3 were redrawn at a high value of Ds, then the magnitudes of pressure difference due to the inertial and Coriolis components can be appreciably large. Returning to the computations of Figure 3, it is found that as γ decreases from a large value, the magnitude of $\Delta\hat{p}_{io,inertia}$ decreases and the magnitude of $\Delta\hat{p}_{io,Coriolis}$ increases, though both trends reverse below certain small values of γ (the reversal in

$\Delta \hat{p}_{io,inertia}$ is visible in Figure 3, and the reversal in $\Delta \hat{p}_{io,Coriolis}$ could be seen if the lower limit of abscissa is extended below 0.53).

$\Delta p_{io,Coriolis}$ depends on the product of V_θ and Ω. With a decrease in $\gamma, \Delta p_{io,Coriolis}$ increases mainly because of an increase in Ω, and below a certain $\gamma, \Delta p_{io,Coriolis}$ decreases mainly because of a decrease in $V_{\theta,i}$ ($V_{\theta,i}$ is the value of V_θ at inlet). However, while estimating $\Delta p_{io,Coriolis}$ one should also take the radial variation of V_θ into account because $\Delta p_{io,Coriolis}$ is an integrated value covering the full radial extent between the inlet and the outlet. Guha and Sengupta[27] explained the fluid dynamics for the radial variation of V_θ at various values of γ. They showed that depending on the relative magnitude of various forces, two different trends are possible in the radial variation of V_θ. In one case, with decreasing radius from the inlet, V_θ decreases to a minimum at a certain radius and then onwards increases. This happens when γ is sufficiently greater than 1. In the other case, V_θ continuously increases with a decrease in radius. This happens either when γ is less than 1 (i.e., the case of flow reversal, see Ref. 27) or when γ is close to 1.

It is to be noted that γ can be interpreted as a Rossby number (a ratio of inertial to Coriolis forces); where, $\bar{U}_{\theta,i}$ and r_i are, respectively, characteristic velocity and length scales. With increasing γ, i.e., increasing Rossby number, the decrease of the Coriolis term and the decrease in the ratio of Coriolis and inertial terms are both consistent with the characteristics of Rossby number. The individual variation of the inertial term is however complex as described above; according to Figure 3, a minima in $\Delta \hat{p}_{io,inertia}$ occur at $\gamma = 1.15$.

We now investigate the role of aspect ratio $\hat{b}$ ($\hat{b} \equiv b/r_i$) while keeping all other non-dimensional numbers fixed. At the first thought, it appears that $\hat{b}$ should also play an important role since the relative proximity of two disc surfaces would influence the value of shear stress and hence the overall fluid dynamics. However, the expression of $\hat{b}$ is included in the definition of Ds [$Ds \equiv (\bar{U}_{r,i}\ b/\nu)(b/r_i) = (\bar{U}_{r,i}\ b/\nu)\hat{b}$]. Since the systematic dimensional analysis of Ref. 26 has produced both Ds and $\hat{b}$ as two separate non-dimensional numbers, we need to reflect on their separate roles. $\hat{b}$ can be altered by varying any or all of b and r_i. Similarly, Ds can be altered by varying any or all of $|\bar{U}_{r,i}|, b, \nu$, and r_i. On the basis of a large number of computational simulations in which Ds and $\hat{b}$ were independently varied over respective relevant ranges, it was found that when $\hat{b}$ is varied but Ds is held constant (by making compensating changes in $\nu, |\bar{U}_{r,i}|$, and b), there is only a little change in the non-dimensional pressure and velocity fields (e.g., in $\hat{p}, \hat{U}_\theta$, or $\hat{U}_r$ as a function of $\hat{z}$ and $\hat{r}$) within the co-rotating discs. A few sample computations to this effect are shown in Table III. Results given in Table III and Figure 2, on the other hand, demonstrate that if $\hat{b}$ is fixed but Ds is varied then large changes happen in the non-dimensional pressure and velocity fields.

Physical intuition tells us that changing the inter-disc spacing b should significantly control the fluid dynamics; it is expected that keeping all other parameters fixed, a reduction in the inter-disc spacing should increase the importance of the viscous force over inertial forces. The discussion in the previous paragraph shows that this primary role of the inter-disc spacing b is contained almost solely in the dynamic similarity number Ds. Although b also appears in another non-dimensional number (the aspect ratio $\hat{b}$), as a direct ratio of b and r_i, the fluid-dynamic role of $\hat{b}$ as a separate non-dimensional number, independent of Ds, is secondary in determining the non-dimensional flow field.

A similitude analysis using the Buckingham's Pi theorem to the present problem[26] has given both Ds and $\hat{b}$ as two independent non-dimensional numbers. From the similitude analysis itself it is not possible to identify their relative importance, and a casual reader could assume that the intuitive feeling about the effect of varying inter-disc spacing is contained in the aspect ratio $\hat{b}$. The systematic computations of the present study have established the primary role of Ds (in which $\hat{b}$ is present as a constituent term) and the secondary role of $\hat{b}$ as a separate non-dimensional number in determining the non-dimensional flow field. This subtle dynamics can also be appreciated from a study of the three momentum equations (4)-(6) in which both Ds and $\hat{b}$ appear as independent parameters, but $\hat{b}$ appears as a squared quantity. Since, for the present physical configuration, $\hat{b}$ is a small quantity, square of $\hat{b}$ is even smaller. This provides the mathematical explanation for why the independent role of $\hat{b}$, outside Ds, on the flow field is secondary.

2. Radial variation of local net pressure difference $\Delta\hat{p}_{net}(r)$ and its components

$\Delta\hat{p}_{net}(r)$ and its components can be determined by changing the upper limit of integration in Equation (2) to the local value of the radius, r, instead of r_o used for the determination of the overall pressure difference discussed in Sec. IV A 1. Figure 4 shows the results of a large number of such numerical integration performed at various r between the inlet and the outlet. It can be seen that with decreasing radius, the magnitude of local net pressure difference monotonically increases. It can also be observed that (at the selected value of γ), with decreasing radius, all four components try to increase the magnitude of pressure difference. In other words, all the components possess the same sign.

The relative magnitudes of the four components of $\Delta\hat{p}_{net}(r)$ depend predominantly on the values Ds and γ selected for the representative computation. Another subtle point is that the sign of the Coriolis component can change (i.e., become positive) over a certain part of the flow field if the value of γ is less than 1. This is so because, with flow reversal, the sign of V_θ is negative over the same certain part of the flow field.

3. The limiting case for zero rotational speed (Ω = 0)

In Section IV A 1, the overall pressure difference was calculated within corotating discs, and many subtle flow physics were discussed. It is interesting to explore the related flow physics for the case of static discs (i.e., $\Omega = 0$ or $\gamma \to \infty$). The same calculation procedure is repeated in order to find the physical mechanism responsible for Δp_{io} in microchannels within static discs. It is to be realised that for the case of static discs, the only non-zero components of the overall pressure difference are $\Delta\hat{p}_{io,inertia}$ and $\Delta\hat{p}_{io,viscous}$. Since γ is not a relevant parameter for the present study, and the computed pressure does not significantly vary with $\hat{b}$, only the effect of change in Ds on the overall pressure difference and on its two relevant components is investigated here (keeping the same values of $\hat{r}_o, \hat{b}$, and α as used in Section IV A 1). In order to generate a high-definition set of comprehensive results, full CFD simulations are run at each of 50 different values of Ds, with appropriate local clustering of data points for higher quantitative resolution in the region of greater qualitative significance. Figure 5 represents the final outcome of this labour-intensive computation. (Note that in addition to the 50 CFD simulations run to obtain Figure 2, 50 more CFD simulations are run to obtain Figure 5.)

Figure 5 shows that the curve corresponding to the variation of $\Delta\hat{p}_{io}$ is bucket-shaped, which is similar to the shape obtained for the case of corotating discs (given in Figure 2). For both small and large values of Ds, the magnitude of $\Delta\hat{p}_{io}$ is large. At a small value of Ds, a large $\Delta\hat{p}_{io}$ occurs because of the large $\Delta\hat{p}_{io,viscous}$; whereas, for large Ds, a large $\Delta\hat{p}_{io}$ occurs because of the large $\Delta\hat{p}_{io,inertia}$. An important difference between the $\Delta\hat{p}_{io}$ versus Ds curve for corotating discs and the $\Delta\hat{p}_{io}$ versus Ds curve for static discs is found in the location of the minima. A comparison between Figures 2 and 5 reveals that the location of minima shifts to a lower value of Ds when the discs are rotating (this happens as the effects of the Coriolis force and the inertia are additive). A quantitative estimate of the shift is from 0.75 (for static discs) to 0.56 (for corotating discs). At the minima, the value of $\Delta\hat{p}_{io}$ for static discs is much lower than that for corotating discs (due to the absence of $\Delta\hat{p}_{io,Coriolis}$ and $\Delta\hat{p}_{io,centrifugal}$).

A study of Equation (2) shows that $\Delta\hat{p}_{io,inertia}$ is composed of several terms; of these, the term containing V_θ^2 is often the dominant term. Now, $V_\theta = U_\theta - \Omega r$ and for the radial inflow simulations, the same value of $U_{\theta,i}$ is used. Thus the magnitude of $\Delta p_{io,inertia}$ is greater for flow through static discs ($\Omega = 0$) than its corresponding magnitude for non-zero rotation; the curves for $\Delta\hat{p}_{io,inertia}$ given in Figures 2 and 5 are consistent with this analysis.

4. A semi-analytical technique for the determination of pressure difference

In this paper, CFD is used for determining the flow field and pressure variation. This is the most general theoretical method. When the inter-disc gap is small, it is shown in Refs. 30 and 33 that it is possible to approximate the z-variations of V_θ and V_r by parabolic profiles. The continuity and momentum equations then give[30,33]

$$\frac{\overline{V}_r(r)}{\overline{V}_{r,i}} = \frac{1}{\hat{r}}, \tag{18}$$

$$\frac{\overline{V}_\theta(r)}{\overline{V}_{\theta,i}} = \frac{\frac{C_2}{C_1} + \left(1 - \frac{C_2}{C_1}\right)\exp\left[\frac{C_1}{2}\left(1-\hat{r}^2\right)\right]}{\hat{r}}, \tag{19}$$

where

$$C_1 = \frac{-10}{Ds},\ C_2 = \frac{-10}{6(\gamma - 1)}. \tag{20}$$

With the help of Equations (2) and (18)-(20), the integral pressure difference equation, keeping only the major contributors based on an order of magnitude analysis,[33] can be written as

$$\begin{aligned}\Delta\hat{p}_{net}(r) &\equiv \frac{\bar{p}(r) - \bar{p}_i}{\rho \bar{U}_{\theta,i}^2}\\ &= \int_1^{\hat{r}} \left[\underbrace{\frac{\hat{r}}{\gamma^2}}_{\boxed{\text{Centrifugal}}} + \underbrace{2\frac{(\gamma-1)}{\gamma^2}\left(\frac{\bar{V}_\theta}{\bar{V}_{\theta,i}}\right)}_{\boxed{\text{Coriolis}}} + \underbrace{\frac{6}{5\hat{r}}\left(\frac{\gamma-1}{\gamma}\right)^2\left(\frac{\bar{V}_\theta}{\bar{V}_{\theta,i}}\right)^2 + \frac{6}{5\hat{r}^3}(\tan\alpha)^2}_{\boxed{\text{Inertia}}} + \underbrace{\frac{12}{\hat{r}}\frac{(\tan\alpha)^2}{Ds}}_{\boxed{\text{Viscous}}}\right] d\hat{r}.\end{aligned} \tag{21}$$

Equation (21) is the same as Equation (18) of Ref. 33, recast in terms of the non-dimensionalization scheme used here. Equation (21) is an ordinary differential equation and can be easily integrated numerically to determine $\Delta\hat{p}_{net}(r)$ (and therefore $\Delta\hat{p}_{io}$ by changing the upper limit $\hat{r}$ by $\hat{r}_o$). The ratio $\bar{V}_\theta/\bar{V}_{\theta,i}$ from Equation (19) needs to be substituted in Equation (21) to get the full form of the integrand. Other than the numerical integration, a series solution of Equation (21) is also possible.[33]

The factor 6/5 appearing in Equation (21) was introduced for the first time in Ref. 33. It arose in Ref. 33 through rigorous mathematical analysis. A physical interpretation was given in Ref. 30 that appropriate use of mass-flow-averaged quantities gives rise to this factor 6/5 for a situation in which strong flow non-uniformities exist in two mutually perpendicular directions. Many researchers inappropriately use area-averaged flow quantities, and then, the factor 6/5 does not occur, with the possibility of producing a large error in the evaluation of work transfer.[30]

The contributions of the four physical mechanisms (viz., centrifugal, Coriolis, inertia, and viscous) are directly attributable to the various terms in the RHS of Equation (21), as shown. All of the qualitative physical reflections on the various terms mentioned after Equation (2) can now be appreciated quantitatively with the help of Equation (21). Equation (21) also contains the basis for changeover of the sign of Coriolis component somewhere in the flow field when $\gamma < 1$. For $\gamma < 1$, $(\gamma - 1)$ is negative, and $\bar{V}_\theta$ also becomes negative (see Equation (19)) in a region close to the inlet causing flow reversal.[27] Therefore, in that region, the product $(\gamma - 1)(\bar{V}_\theta/\bar{V}_{\theta,i})$ becomes negative changing the sign of the Coriolis component in the reversed flow region. The tangential speed ratio at inlet, γ, and the ratio $\bar{V}_\theta/\bar{V}_{\theta,i}$, on the other hand, appear as squared quantities in the inertia term; hence, the sign of the inertia term does not depend on the value of γ.

The specialized form of Equation (21) for the case of static discs can be obtained by taking the limit $\gamma \to \infty$ on Equation (21), the final equation being,

$$\Delta\hat{p}_{net}(r)\big|_{static\ discs} \equiv \left.\frac{\bar{p}(r) - \bar{p}_i}{\rho\bar{U}_{\theta,i}^2}\right|_{static\ discs} = \int_1^{\hat{r}} \left[\frac{6}{5\hat{r}}\left(\frac{\bar{V}_\theta}{\bar{V}_{\theta,i}}\right)^2 + \frac{6}{5\hat{r}^3}(\tan\alpha)^2 + \frac{12}{\hat{r}}\frac{(\tan\alpha)^2}{Ds}\right] d\hat{r}. \tag{22}$$

Equations (21) and (22) are mentioned here for the sake of completeness. The above procedure can be applied to easily derive equations equivalent to (21) and (22) for the radial outflow arrangement. We, however, return to the use of CFD for solving the radial outflow arrangement in Section IV B.

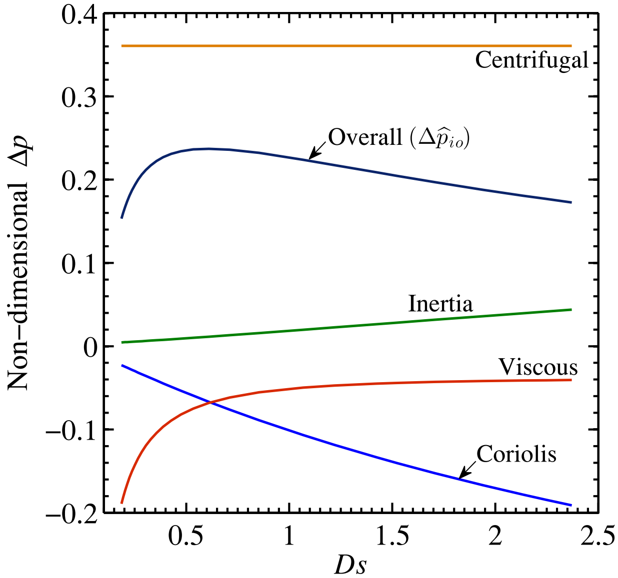

FIG. 6. Contribution of various forces to produce the overall radial pressure difference $\Delta\hat{p}_{io}$ over a range of dynamic similarity number Ds: prediction of the present CFD simulations for radial outflow. ($\hat{r}_i = 0.528$, $\hat{b} = 0.008$, $\phi = 0.124$, and uniform velocity distribution at inlet: $U_{r,i} = \bar{U}_{r,i}$. Pressure differences are non-dimensionalized by $\rho\Omega^2 r_o^2$. Each curve contains data from 50 separate CFD simulations, with appropriate higher resolution close to the maxima.)

B. Radial outflow arrangement

Figure 1 shows the physical configuration and Figures 6-9 show representative results for the radial outflow case. It is found that for this case also the role of $\hat{b}$ as a separate non-dimensional number, independent of Ds, is secondary in determining the non-dimensional flow field. It is already mentioned that from practical considerations, the flow angle at inlet α is fixed at 90°. The radius ratio is kept fixed at its previous value, i.e., $\hat{r}_i = 0.528$. Additional computations for other

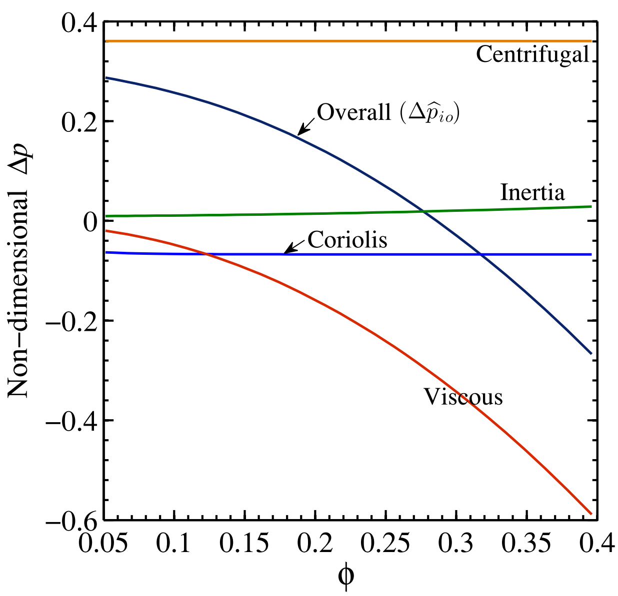

FIG. 7. Contribution of various forces to produce the overall radial pressure difference $\Delta\hat{p}_{io}$ over a range of flow coefficient at inlet ϕ: prediction of the present CFD simulations for radial outflow. ($\hat{r}_i = 0.528, \hat{b} = 0.008, Ds = 0.61$, and uniform velocity distribution at inlet: $U_{r,i} = \bar{U}_{r,i}$. Pressure differences are non-dimensionalized by $\rho\Omega^2 r_o^2$. Each curve contains data from 50 separate CFD simulations.)

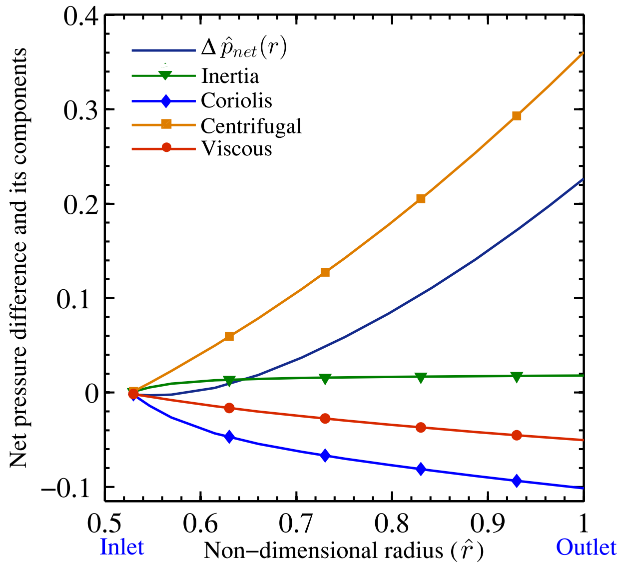

FIG. 8. Radial variation of local net pressure difference $\Delta\hat{p}_{net}(r)$ and its components: prediction of the present CFD simulations for radial outflow. ($\hat{r}_i = 0.528, \hat{b} = 0.008, Ds = 1, \phi = 0.124$, and uniform velocity distribution at inlet: $U_{r,i} = \bar{U}_{r,i}$. Pressure differences are non-dimensionalized by $\rho\Omega^2 r_o^2$. There are 125 grid points between the inlet and the outlet.)

values of $\hat{r}_i$, not reported here, showed that they do not reveal any new physics. We therefore focus our attention to the two remaining, most important, non-dimensional numbers Ds and ϕ.

Table I shows that for the case of corotating discs with radial outflow, quantities like pressure and pressure difference are non-dimensionalized by $\rho\Omega^2 r_o^2$. As a result, the non-dimensional centrifugal component becomes a function of r_i alone, the relation being $\Delta\hat{p}_{io,centrifugal} = (1 - \hat{r}_i^2)/2$.

The present section is divided into three subsections. Section IV B 1, with Figures 6 and 7, gives the physical mechanisms of the overall radial pressure difference (Δp_{io}). Section IV B 2, with Figure 8, presents the physical mechanisms of the variation in local net pressure difference $\Delta p_{net}(r)$.

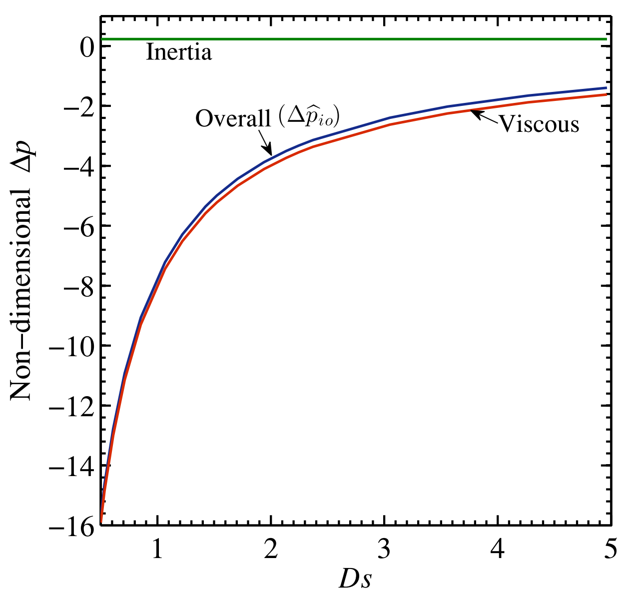

FIG. 9. Contribution of various forces within two static discs to produce the overall radial pressure difference $\Delta\hat{p}_{io}$ over a range of dynamic similarity number Ds: prediction of the present CFD simulations for radial outflow. ($\hat{r}_i = 0.528, \hat{b} = 0.008$, and uniform velocity distribution at inlet: $U_{r,i} = \bar{U}_{r,i}$. Pressure differences are non-dimensionalized by $\rho\bar{U}_{r,i}^2$. Each curve contains data from 50 separate CFD simulations.)

Section IV B 3, with Figure 9, provides a discussion on the baseline solutions when the discs are static.

1. Physical mechanisms for the overall pressure difference, $\Delta\hat{p}_{io}$

At first, we explore the role of Ds while keeping all other non-dimensional numbers fixed. In order to generate a high-definition set of comprehensive results, full CFD simulations are run at each of 50 different values of Ds, with appropriate local clustering of data points for higher quantitative resolution in the region of greater qualitative significance.

Figure 6 shows the variation of $\Delta\hat{p}_{io}$ and its four components $\Delta\hat{p}_{io,inertia}$, $\Delta\hat{p}_{io,Coriolis}$, $\Delta\hat{p}_{io,centrifugal}$, and $\Delta\hat{p}_{io,viscous}$ with Ds. The positive values of $\Delta\hat{p}_{io}$ indicate that pressure increases from the inlet to the outlet. It can be observed that the curve corresponding to the variation of $\Delta\hat{p}_{io}$ is inverted bucket-shaped and $\Delta\hat{p}_{io}$ is maximum at a certain Ds (around 0.6 for the present case). The physical reason behind the inverted bucket-shape of $\Delta\hat{p}_{io}$ versus Ds curve can be understood in terms of the quantitative variation of the four components of $\Delta\hat{p}_{io}$. First of all, consider the sign of the four components. It is found that $\Delta\hat{p}_{io,centrifugal}$ and $\Delta\hat{p}_{io,inertia}$ are positive, whereas $\Delta\hat{p}_{io,Coriolis}$ and $\Delta\hat{p}_{io,viscous}$ are negative. $\Delta\hat{p}_{io,centrifugal}$ is positive because $\hat{r}_i$ is less than 1 [$\Delta\hat{p}_{io,centrifugal} = (1-\hat{r}_i^2)/2$]. $\Delta\hat{p}_{io,inertia}$ is positive because $\rho V_\theta^2/r$ and $-\rho V_r/(\partial V_r/\partial r)$ are positive and the term $-\rho V_z/(\partial V_r/\partial z)$ is very small. $\Delta\hat{p}_{io,viscous}$ is negative because fluid friction always causes pressure drop. $\Delta\hat{p}_{io,Coriolis}$ is negative because for radial outflow, V_θ is negative (except at the solid walls where V_θ is zero due to no slip condition). Secondly, we consider the magnitude of the positive components. It is found that $\Delta\hat{p}_{io,inertia}$ is small, especially at small Ds. On the contrary, $\Delta\hat{p}_{io,centrifugal}$ has a dominating effect. $\Delta\hat{p}_{io,centrifugal}$ depends only on the radius ratio and thus remains constant when only Ds is varied. Thirdly, we reflect upon the magnitude of the negative components. At a small value of Ds, the magnitude of $\Delta\hat{p}_{io,viscous}$ is large but the magnitude of $\Delta\hat{p}_{io,Coriolis}$ is small. On the contrary, at a large Ds, the magnitude of $\Delta\hat{p}_{io,Coriolis}$ is large but $\Delta\hat{p}_{io,viscous}$ is small. As a result of the above-mentioned signs and relative magnitudes of the components, two interesting features arise in the overall radial pressure difference: (i) the magnitude of $\Delta\hat{p}_{io}$ is less than that of the centrifugal component $\Delta\hat{p}_{io,centrifugal}$ alone and (ii) $\Delta\hat{p}_{io}$ exhibits a maxima at a certain value of Ds.

From the above list of observations, it can be inferred that at a small value of Ds, a small $\Delta\hat{p}_{io}$ occurs because of the large magnitude of $\Delta\hat{p}_{io,viscous}$ which opposes $\Delta\hat{p}_{io,centrifugal}$. On the other hand, at a comparatively greater Ds, a small $\Delta\hat{p}_{io}$ occurs because of the large magnitude of $\Delta\hat{p}_{io,Coriolis}$ which opposes $\Delta\hat{p}_{io,centrifugal}$. Furthermore, for a decrease of Ds from $Ds \approx 0.6$, the decrement of $\Delta\hat{p}_{io}$ is drastic due to the sharp rise of the magnitude of $\Delta\hat{p}_{io,viscous}$. On the other hand, for an increase of Ds from $Ds \approx 0.6$, the decrement of $\Delta\hat{p}_{io}$ is rather slow because of two reasons. The rate of increase of the magnitude of $\Delta\hat{p}_{io,Coriolis}$ is not drastic and $\Delta\hat{p}_{io,inertia}$ increases. This subtle fluid dynamics is responsible for the special shape of $\Delta\hat{p}_{io}$ versus Ds curve as shown in Figure 6.

We now investigate the role of ϕ while keeping all other non-dimensional numbers fixed. ϕ is defined as: $\phi = \bar{U}_{r,i}/(\Omega r_i)$. The radial velocity at the inlet of the rotor, $\bar{U}_{r,i}$, is fixed for maintaining a specific flow rate, and r_i is fixed for a particular rotor. Therefore, in order to understand the fluid dynamics of the rotational flow, ϕ in the illustrative computations of this study is varied by altering the rotational speed Ω. In the abscissa of Figure 7, increasing ϕ therefore also equivalently represents decreasing Ω. This should be kept in mind while interpreting the variations of various non-dimensional quantities of Figure 7 since quantities like pressure and pressure difference are non-dimensionalized, for the radial outflow case, by $\rho\Omega^2 r_o^2$.

Figure 7 is obtained by running full CFD simulations at each of 50 different values of ϕ. Figure 7 shows the variation of $\Delta\hat{p}_{io}$ and its four components $\Delta\hat{p}_{io,inertia}$, $\Delta\hat{p}_{io,Coriolis}$, $\Delta\hat{p}_{io,centrifugal}$, and $\Delta\hat{p}_{io,viscous}$ with ϕ. With an increase in ϕ, $\Delta\hat{p}_{io}$ decreases, and the value of $\Delta\hat{p}_{io}$ changes from positive to negative. The physical reason behind the above trend of $\Delta\hat{p}_{io}$ can be understood in terms of the quantitative variation of the four components of $\Delta\hat{p}_{io}$. It is discussed previously that $\hat{p}_{io,centrifugal}$ and $\Delta\hat{p}_{io,inertia}$ are positive, whereas $\Delta\hat{p}_{io,Coriolis}$ and $\Delta\hat{p}_{io,viscous}$ are negative (see Figure 7). $\Delta\hat{p}_{io,centrifugal}$ remains constant with varying ϕ because it depends only on the radius ratio. At small ϕ, $\Delta\hat{p}_{io,centrifugal}$ becomes the major contributor and $\Delta\hat{p}_{io,viscous}$, $\Delta\hat{p}_{io,inertia}$, and $\Delta\hat{p}_{io,Coriolis}$ are small. Consequently, $\Delta\hat{p}_{io}$, is positive. At large ϕ, $\Delta\hat{p}_{io,viscous}$ becomes the major contributor, hence, $\Delta\hat{p}_{io}$ becomes negative.

It is to be noted $\Delta\hat{p}_{io,Coriolis}$ [$\Delta\hat{p}_{io,Coriolis} \equiv \int_{r_i}^{r_o} \left((1/b)\int_0^b (2\rho V_\theta)\, dz\right) dr/(\rho\Omega r_o^2)$] changes insignificantly with an increase in ϕ. It is already mentioned that ϕ is varied here by changing Ω. With an increase in ϕ (i.e., decrease in Ω), it can be shown that the magnitude of V_θ decreases. Thus, in the expression of $\Delta\hat{p}_{io,Coriolis}$, both the numerator and the denominator decrease with an increase in ϕ. This may explain the presented trend of $\Delta\hat{p}_{io,Coriolis}$. For the selected fixed value of Ds, $\Delta\hat{p}_{io,inertia}$ is small which is consistent with the message contained in Figure 6. Figure 6 shows that for small and moderate values of Ds, $\Delta\hat{p}_{io,inertia}$ is small.

It is already stated that $\Delta\hat{p}_{io}$ for radial outflow may be positive or negative. The implication of the negative $\Delta\hat{p}_{io}$ is that the power, from an external source, is required not only to maintain a steady disc-speed Ω but also to maintain a constant positive head at the rotor inlet for sustaining a steady radial efflux. On the other hand, the positive $\Delta\hat{p}_{io}$ implies that the externally supplied power is solely utilized to maintain a steady disc-speed Ω which, in turn, causes a continuous pumping action in a radially outward direction and gives rise to an increase in pressure from inlet to outlet. Therefore, for a positive $\Delta\hat{p}_{io}$, this radial outflow device may act as a pump. The largest possible positive value of $\Delta\hat{p}_{io}$ is $(1 - \hat{r}_i^2)/2$, which is the value of $\Delta\hat{p}_{io,centrifugal}$ (see Figure 7).

2. Radial variation of local net pressure difference $\Delta\hat{p}_{net}(r)$ and its components

$\Delta\hat{p}_{net}(r)$ and its components can be determined by changing the upper limit of integration in Equation (2) to the local value of the radius, r, instead of r_o used for the determination of the overall pressure difference discussed in Sec. IV B 1. Figure 8 shows the radial variation of the local net pressure difference and its components. It is observed that close to the inlet, the net pressure difference is negative. However, with an increase in non-dimensional radius, the net pressure difference changes its sign and becomes positive (at the selected value of ϕ). Therefore, at some intermediate non-dimensional radius between inlet and outlet, the net pressure difference is zero. The radial location of zero net pressure-difference depends on the values of the fixed non-dimensional numbers. It is to be observed that centrifugal and inertial components of the net pressure are positive, whereas Coriolis and viscous components of the net pressure are negative. Explanations related to the sign of the components are provided in Sec. IV B 1. Close to the inlet, the combined effect of Coriolis and viscous components overtakes the effect of centrifugal and inertial components. Therefore, the sign of the net pressure difference is negative. With an increase of radius, the influence of the centrifugal component increases, so much so that the net pressure difference becomes positive.

Figure 7 shows that at large values of ϕ (i.e., at small values of rotational speed Ω), $\Delta\hat{p}_{io}$ can be negative. If Figure 8 were redrawn at such values of ϕ, $\Delta\hat{p}_{net}(r)$ may remain negative at all radii from the inlet to the outlet.

3. The limiting case for zero rotational speed ($\Omega = 0$)

The limiting case for zero rotational speed (i.e., static discs) is also investigated. A summary of results is described below. When the discs are static, ϕ tends to ∞. We, therefore, examine only the effect of change in Ds on the overall pressure difference. Figure 9 is based on labour-intensive computations in which full CFD simulations are run at each of 50 different values of Ds. (Note that in addition to the 50 CFD simulations run to obtain Figure 6, 50 more CFD simulations are run to obtain Figure 9.)

It is found that the overall pressure difference is negative and its magnitude decreases with increasing Ds, unless Ds is very large. In the absence of rotation, both centrifugal and Coriolis components are zero and viscous and inertial components are the only active parts. The inertial component is positive but its contribution is small unless Ds is very large. The viscous component is negative (unless at very large Ds) and makes the dominating contribution to the overall pressure difference whose sign, magnitude, and the trend of variation as Ds changes are all close to those of the viscous component. The shape of the $\Delta\hat{p}_{io}$ versus Ds curve for the static discs is thus similar to that of the $\Delta\hat{p}_{io,viscous}$ versus Ds curve shown in Figure 6. Unlike the case of corotating discs (see

Figure 2 or 6) or static discs with radial inflow (Figure 5), the curve of the overall pressure difference for static discs with radial outflow does not pass through any extrema. It is so because with increasing Ds, the values (not the magnitudes) of both viscous and inertial components increase. Since Ω is zero, $\rho\bar{U}_{r,i}^2$, instead of $\rho\Omega^2 r_o^2$, may be used for non-dimensionalising the pressure differences.

A study of Equation (2) shows that $\Delta p_{io,inertia}$ is composed of several terms; of these, the term containing V_θ^2 is often the dominant term. Now, $V_\theta = U_\theta - \Omega r$ and for the radial outflow simulations, the assumed value of $U_{\theta,i}$ is zero. Thus, for static discs ($\Omega = 0$), $V_\theta = 0$. The magnitude of $\Delta p_{io,inertia}$, for flow through static discs with radial outflow, is therefore quite small, and the variation in $\Delta\hat{p}_{io}$ closely resembles that in $\Delta\hat{p}_{io,viscous}$ (as seen in Figure 9).

V. CONCLUSION

In this paper, a new formulation is presented for understanding the radial pressure variation for flow through microchannels within corotating or static discs. The full benefit of similitude and scaling is extracted by expressing the results and analyses in terms of carefully formulated non-dimensional numbers. We have given emphasis not only on the overall magnitude of the radial pressure difference (Δp_{io}) but also on the mechanisms of pressure variation, and with this objective, the separate roles of inertia, centrifugal force, Coriolis force, and viscous effects are determined quantitatively. The present paper demonstrates that the aspect ratio ($\hat{b}$) plays only a secondary role as an independent parameter, its major role being contained within the newly identified dynamic similarity number (Ds). For radial inflow, it is established that $\Delta\hat{p}_{io,viscous}$ depends predominately on Ds; $\Delta\hat{p}_{io,centrifugal}$ depends predominately on γ; and $\Delta\hat{p}_{io,inertia}$ and $\Delta\hat{p}_{io,Coriolis}$ depend on both Ds and γ (see Figures 2 and 3). It is shown that the magnitude of Δp_{io} decreases monotonically as the tangential speed ratio (γ) increases, and the centrifugal force is dominant at low γ. Δp_{io} exhibits a minima when Ds is varied, viscous effects dominating at low Ds, while Coriolis force and inertia dominating at large Ds. For radial outflow, $\Delta\hat{p}_{io,centrifugal}$ and $\Delta\hat{p}_{io,inertia}$ are positive, whereas $\Delta\hat{p}_{io,Coriolis}$ and $\Delta\hat{p}_{io,viscous}$ are negative and $\Delta\hat{p}_{io}$ may be either positive or negative depending on the quantitative variation of these four components. It is demonstrated that $\Delta\hat{p}_{io}$ increases monotonically as the flow coefficient (ϕ) decreases but evinces a maxima when Ds is varied. The occurrence of these extrema (i.e., the minima for radial inflow devices and maxima for radial outflow devices) offers the scope for the optimization of macrofluidic and microfluidic devices consisting of corotating discs.

Computations for the limiting cases with zero rotational speed ($\Omega = 0$) show that there is no extrema in the Δp_{io} versus Ds curve for the radial outflow case, but for the radial inflow case, the inertia and viscous components bring about a minima in the magnitude of Δp_{io} as Ds is varied. As compared to the corotating discs, the minima occur at a greater value of Ds and the magnitude of Δp_{io} is a lot smaller at the point of minima. These changes are caused by the absence of the centrifugal and Coriolis components in the case of static discs.

[1] M. Avila, "Stability and angular-momentum transport of fluid flows between corotating cylinders," Phys. Rev. Lett. **108**(12), 124501 (2012).
[2] S. Xu and A. Nadim, "Oscillatory counter-centrifugation," Phys. Fluids **28**(2), 021302-1–021302-20 (2016).
[3] G. P. Hoya and A. Guha, "The design of a test rig and study of the performance and efficiency of a Tesla disc turbine," Proc. Inst. Mech. Eng., Part A **223**(4), 451–465 (2009).
[4] Y. Burnishev and V. Steinberg, "Influence of polymer additives on turbulence in von Karman swirling flow between two disks. II," Phys. Fluids **28**(3), 033101-1–033101-31 (2016).
[5] A. Guha and B. Smiley, "Experiment and analysis for an improved design of the inlet and nozzle in Tesla disc turbines," Proc. Inst. Mech. Eng., Part A **224**(2), 261–277 (2010).
[6] S. Sengupta and A. Guha, "Flow of a nanofluid in the microspacing within co-rotating discs of a Tesla turbine," Applied Mathematical Modelling **40**(1), 485–499 (2016).
[7] F. Marques and J. M. Lopez, "Precession of a rapidly rotating cylinder flow: Traverse through resonance," J. Fluid Mech. **782**, 63–98 (2015).
[8] H. P. Greenspan, *The Theory of Rotating Fluids* (Cambridge University Press, Cambridge, UK, 1968).
[9] J. M. Owen and R. H. Rogers, *Flow and Heat Transfer in Rotating Disc Systems, Vol. 1: Rotor-Stator Systems* (Research Studies Press, Taunton, UK, 1989).
[10] P. R. N. Childs, *Rotating Flow* (Butterworth-Heinemann Press, Oxford, UK, 2011).

[11] J. P. Vanyo, *Rotating Fluids in Engineering and Science* (Butterworth-Heinemann Press, Stoneham, MA, USA, 2015).
[12] T. von Kármán, "Über läminare und turbulence Reibung," Z. Angew. Math. Mech. **1**, 233–252 (1921).
[13] U. T. Bödewadt, "Die Drehströmung über festem Grunde," Z. Angew. Math. Mech. **20**, 241–253 (1940).
[14] G. K. Batchelor, "Note on a class of solutions of the Navier-Stokes equations representing steady rotationally-symmetric flow," Q. J. Mech. Appl. Math. **4**, 29–41 (1951).
[15] K. Stewartson, "On the flow between two rotating coaxial disks," Proc. Cambridge Philos. Soc. **49**, 333–341 (1953).
[16] A. Guha and S. Sengupta, "Analysis of von Kármán's swirling flow on a rotating disc in Bingham fluids," Phys. Fluids **28**(1), 013601-1–013601-30 (2016).
[17] R. J. Lingwood and P. H. Alfredsson, "Instabilities of the von Karman boundary layer," Appl. Mech. Rev. **67**(3), 030803 (2015).
[18] S. J. Garrett, A. J. Cooper, J. H. Harris, M. Özkan, A. Segalini, and P. J. Thomas, "On the stability of von Kármán rotating-disk boundary layers with radial anisotropic surface roughness," Phys. Fluids **28**(1), 014104-1–014104-18 (2016).
[19] S. O. MacKerrell, "Stability of Bödewadt flow," Philos. Trans. R. Soc. London, Ser. A **363**(1830), 1181–1187 (2005).
[20] J. M. Lopez, F. Marques, A. M. Rubio, and M. Avila, "Crossflow instability of finite Bödewadt flows: Transients and spiral waves," Phys. Fluids **21**(11), 114107 (2009).
[21] Y. Do, J. M. Lopez, and F. Marques, "Optimal harmonic response in a confined Bödewadt boundary layer flow," Phys. Rev. E **82**(3), 036301 (2010).
[22] E. Serre, E. C. D. Arco, and P. Bontoux, "Annular and spiral patterns in flows between rotating and stationary discs," J. Fluid Mech. **434**, 65–100 (2001).
[23] K. M. P. van Eeten, J. van der Schaaf, J. C. Schouten, and G. J. F. van Heijst, "Boundary layer development in the flow field between a rotating and a stationary disk," Phys. Fluids **24**(3), 033601-1–033601-18 (2012).
[24] S. Poncet, M. P. Chauve, and R. Schiestel, "Batchelor versus Stewartson flow structures in a rotor-stator cavity with through-flow," Phys. Fluids **17**, 075110 (2005).
[25] B. Launder, S. Poncet, and E. Serre, "Laminar, transitional, and turbulent flows in rotor-stator cavities," Ann. Rev. Fluid Mech. **42**, 229–248 (2010).
[26] A. Guha and S. Sengupta, "Similitude and scaling laws for the rotating flow between concentric discs," Proc. Inst. Mech. Eng., Part A **228**(4), 429–439 (2014).
[27] A. Guha and S. Sengupta, "The fluid dynamics of the rotating flow in a Tesla disc turbine," Eur. J. Mech., B: Fluids **37**, 112–123 (2013).
[28] Y. Omi and R. Iwatsu, "Numerical study of swirling flows in a cylindrical container with co-/counter-rotating end disks under stable temperature difference," Int. J. Heat Mass Transfer **48**(23), 4854–4866 (2005).
[29] B. Herrmann-Priesnitz, W. R. Calderón-Muñoz, E. A. Salas, A. Vargas-Uscategui, M. A. Duarte-Mermoud, and D. A. Torres, "Hydrodynamic structure of the boundary layers in a rotating cylindrical cavity with radial inflow," Phys. Fluids **28**(3), 033601-1–033601-16 (2016).
[30] A. Guha and S. Sengupta, "The fluid dynamics of work transfer in the non-uniform viscous rotating flow within a Tesla disc turbomachine," Phys. Fluids **26**(3), 033601-1–033601-27 (2014).
[31] C. Y. Soong, C. C. Wu, T. P. Liu, and T. P. Liu, "Flow structure between two co-axial disks rotating independently," Exp. Therm. Fluid Sci. **27**(3), 295–311 (2003).
[32] E. Lemma, R. T. Deam, D. Toncich, and R. Collins, "Characterisation of a small viscous flow turbine," Exp. Therm. Fluid Sci. **33**, 96–105 (2008).
[33] S. Sengupta and A. Guha, "A theory of Tesla disc turbines," Proc. Inst. Mech. Eng., Part A **226**(5), 650–663 (2012).
[34] Fluent 6.3 User's Guide, Fluent, Inc., Central Source Park, 10 Cavendish Court, Lebanon, NH 03766, USA, 2006.
[35] S. V. Patankar, *Numerical Heat Transfer and Fluid Flow* (Hemisphere, Washington, DC, 1980).
[36] Y. Mei and A. Guha, "Implicit numerical simulation of transonic flow through turbine cascades on unstructured grids," Proc. Inst. Mech. Eng., Part A **219**(A1), 35–47 (2005).